

Lattice Vibrational Modes in Si/Ge Core-shell Nanowires

Shouting Huang and Li Yang

Department of Physics, Washington University, St. Louis, Missouri 63130, USA

(Dated: November 16, 2018)

We present a first-principles study on lattice vibrational modes of Si/Ge core-shell nanowires (NWs). In addition to quantum confinement, the internal strain induced by the lattice mismatch between core and shell contributes to significant frequency shifts of characteristic optical modes. More importantly, our simulation shows that these frequency shifts can be detected by Raman scattering experiments, providing convenient and nondestructive ways to obtain structural information of core-shell materials. Meanwhile, another type of collective modes, radial breathing modes (RBMs), are identified in Si-core/Ge-shell NWs and their frequency dependence is explained by an elastic media model.

I. INTRODUCTION

Core-shell nanowires (NWs), a type of novel quasi-one-dimensional nanostructures, have ignited tremendous interest to date because these unique radial heterojunctions own extra degrees of freedom to tune the mechanical, electric and optical properties by varying their core and shell sizes, respectively, which make them superior to usual homogenous materials¹⁻⁴. Among numerous core-shell structures, Si/Ge core-shell NWs are of particular interest because of the known importance of silicon on microelectronics. Recent research has shown that Si/Ge core-shell NWs own a number of unusual thermal transport features for energy applications⁵⁻⁷. For example, the enhanced difference in thermal and electric transport behaviors between the core and shell gives rise to higher-efficiency thermoelectric devices based on core-shell NWs⁸.

In order to realize and optimize the above interesting properties, it is imperative to determine how to obtain structural information and, thereafter, how to design core and shell geometries. Traditional approaches, such as the transmission electron microscopy (TEM) and neutron scattering measurements, are time consuming or expensive for the large-scale production; alternative convenient ways are highly desired. On the other hand, lattice vibrational modes are known to be sensitive to the chemical bonding and boundary conditions of nanostructures and they are well accessible by varieties of experiments, such as Raman scattering^{9,10,12}, making it possible to study lattice vibrational modes of core-shell NWs and extract useful structural information.

Beyond application interests, lattice vibrational modes and corresponding phonons are fundamental properties of solids. However, compared with bulk semiconductors and homogenous nanostructures, there have been very limited first-principles studies on vibrational modes of core-shell NWs although the core-shell structure will surely introduce richer physics. Therefore, calculating lattice vibrational modes in Si/Ge core-shell NWs will be an appropriate starting point to understand electric and thermal properties of reduced dimensional structures.

In this work, we employ first-principles calculations and focus on the following two topics of Si/Ge core-shell

NWs: 1) how the unique core-shell structure modifies lattice vibrational modes and what their impacts on thermal properties are; 2) how to extract the structural information from characters of lattice vibrational modes and provide clues for experimental measurements.

Through our simulations, we find that the structural information of core-shell NWs can be efficiently obtained by frequency shifts of high-energy optical vibrational modes. This type of frequency shifts can be well explained by the change of the strain induced by the lattice mismatch between the core and shell. Moreover, we have calculated the Raman scattering spectrum of Si/Ge core-shell NWs, showing that these frequency shifts can be detected by experiments. Meanwhile, we identify the existence of RBMs in Si-core/Ge-shell NWs, whose frequency variation can be understood by an elastic media model.

The rest of this article is organized as the following. In Sec. II, we present our calculation methodology and computational setup. In Sec. III, we discuss the simulation results, including properties of high-frequency optical modes, Raman scattering spectra, and the RBM frequency dependence on the structure of core-shell NWs. In Sec. IV, we summarize our studies and conclusion.

II. COMPUTATIONAL DETAILS

Our calculation is based on the density functional theory (DFT) within the local density approximation (LDA)^{14,15} as implemented in the Quantum ESPRESSO package¹⁶. We employ the plan-wave basis and the pseudopotential approximation¹⁸. The plane-wave energy cutoff is 16 Ry. For the Brillouin zone (BZ) integration, we use a $1 \times 1 \times 8$ k-point sampling grid. All calculations are done in a supercell arrangement¹⁷ with a 0.7-nm vacuum distance between neighboring NWs. Our studied NWs are oriented along the [110] direction, an energetically preferred configuration¹⁹. Those dangling bonds on the surface of NWs are passivated by hydrogen atoms. All NWs are fully relaxed according to the force and stress calculated under DFT/LDA.

There are a number of degrees of freedom to decide the structure of core-shell NWs, such as the core size, shell

TABLE I: The structure information of Si/Ge core-shell NWs and homogenous NWs investigated. (SiGe means Si core and Ge shell while GeSi means Ge core and Si shell.)

NWs	Core	Shell	Core diameter (nm)	Shell diameter (nm)	Lattice constant along wire (nm)
Si-1	Si	Si	2.24	2.24	0.378
GeSi-1	Ge	Si	1.12	2.21	0.383
GeSi-2	Ge	Si	1.75	2.30	0.390
Ge-1	Ge	Ge	2.41	2.41	0.401
SiGe-1	Si	Ge	1.09	2.33	0.396
SiGe-2	Si	Ge	1.66	2.29	0.388
Si-2	Si	Si	1.61	1.61	0.382
Ge-2	Ge	Ge	1.76	1.76	0.405

size and the chemical compositions. Because it is impossible to study all of them in one article, we investigate Si/Ge core-shell NWs with a fixed diameter (~ 2.3 nm) but a varying core-shell size ratio. At the same time, homogenous NWs are also studied for comparison purposes. The detailed structural information of our studied NWs is reported in Table I.

We employ the linear response approach to obtain lattice vibrational modes and their frequencies^{20–23}. Only vibrational modes at the Γ point of the first BZ is calculated because it is of particular interest for the first-order Raman scattering measurement.

We calculate the Raman scattering spectrum by considering the non-resonant first-order process, which can be described within the Placzek approximation^{24,25}. Then the Raman activity I_{ramman}^k associated with the vibrational mode k is

$$I_{ramman}^k = |e_s \cdot \alpha^k \cdot e_L|, \quad (1)$$

where e_s is the polarization of incoming photon and e_L is the polarization of scattered outgoing photon. The Raman tensor α^k is defined as

$$\alpha^k = \sqrt[2]{\Omega} \sum_{al} \frac{\partial \chi_{ij}}{\partial r_{al}} u_{al}^k, \quad (2)$$

where χ_{ij} is the electric polarizability tensor, a is the index to specify the atom in the unit cell, and l is the index of coordinates. u_{al}^k is the displacement of the atom a along l direction in the vibrational eigenmode k .

For realistic experimental cases, NWs are usually oriented randomly. Because of the depolarization effect, we may only consider the circumstances that the direction of the incident beam, the polarization direction of this beam, and the direction of the observation are perpendicular to each other. Then the spatially averaged Raman activity of those randomly orientated NWs is given by:

$$I_{ramman}^k = 5(\alpha_{xx}^k + \alpha_{yy}^k + \alpha_{zz}^k)^2 + \frac{7}{4}[(\alpha_{xx}^k - \alpha_{yy}^k)^2 + (\alpha_{xx}^k - \alpha_{zz}^k)^2 + (\alpha_{yy}^k - \alpha_{zz}^k)^2 + 6(|\alpha_{xy}^k|^2 + |\alpha_{xz}^k|^2 + |\alpha_{yz}^k|^2)]. \quad (3)$$

Because our calculated Raman spectra only consider the first-order process, they may be different from some Raman experiments which could be dominated by resonant effects. However, our obtained Raman activity, *e.g.*, active or not, shall still be useful to understand those resonant experiments.

III. RESULTS AND DISCUSSIONS

A. High-frequency optical modes

The density of vibrational modes (DVM) at the Γ point is presented in Fig. 1. It has to be pointed out that those vibrational modes mainly consisting of hydrogen-atom motions are excluded from our plots because we are

interested in intrinsic vibrational modes of NWs that are not sensitive to the environment. Therefore, our results and conclusion will be more universal and less influenced by complicated passivations as in various experiments.

The most prominent feature of these DVMs is that there are two characteristic peaks among most core-shell NWs, which are marked by O_{Si} and O_{Ge} in Fig. 1, respectively. To understand the physical origin of these peaks, we have plotted the real-space motion of two typical modes corresponding to these peaks in Fig. 2.

The first character of these modes is that they are mainly confined within the core or shell, respectively. In another word, these Si and Ge vibrational modes are decoupled. For example, Fig. 2 (a) is mainly the Si-Si vibrational mode confined within the core regime while Fig. 2 (b) is mainly the Ge-Ge mode within the shell

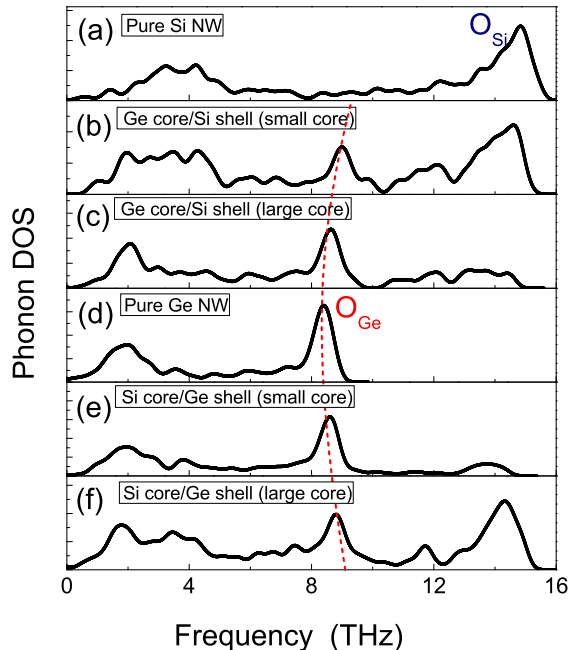


FIG. 1: DVM at the Γ point of Si/Ge core-shell NWs and homogenous NWs with wire diameter of about 2.3 nm in Table I. (a) Si-1 NW (b) GeSi-1 NW (c) GeSi-2 NW (d) Ge-1 NW (e) SiGe-1 NW (f) SiGe-2 NW. The red dashed line is used to guide the shift trend of the peak of high-frequency Ge-Ge optical modes.

regime. This decoupling is due to the significant mass difference between Si and Ge atoms and their bonding strength differences.

The second character is that the neighboring atoms of these modes plotted in Fig. 2 have opposite vibrational directions, a typical feature of optical modes of semiconductors at the Γ point. Based on the above two characters, we conclude that these peaks (O_{Si} and O_{Ge}) originate from those high-frequency optical modes of bulk Si and Ge. This can be further confirmed by their frequency; the O_{Ge} peak has a frequency around 8 THz while the O_{Si} peak has a frequency around 15 THz. They are consistent with frequencies of optical modes in Si and Ge bulk crystals.

However, the frequencies of peaks (O_{Ge} and O_{Si}) are not exactly the same as their bulk counterparts. Instead they exhibit substantial frequency shifts as the core-shell size varies as shown in Fig. 1. For example, as we expand the Ge-core size from zero to the whole Ge-core/Si-shell wire (Figs. 1 (a) to (d)), both peaks O_{Si} and O_{Ge} have a red shift. Similarly, both peaks have a blue shift as Si core size increases in the case of Si-core/Ge-shell NWs, as shown in Figs. 1 (d) to (f).

The physical origin of the above shifts of prominent

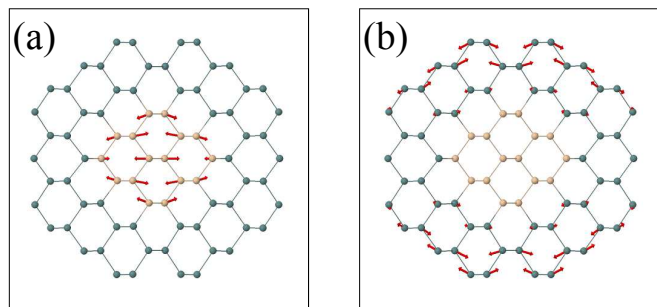


FIG. 2: The typical vibrations of highest-frequency optical modes in Si/Ge core-shell NWs. Hydrogen atoms on the surface are not plotted. The arrows stand for the motion direction and magnitude. (a) The highest-frequency Si optical mode in the O_{Si} peak of a Si-core/Ge-shell NW. (b) The highest-frequency Ge optical mode in the O_{Ge} peak of the Si-core/Ge-shell NW.

peaks in the DVM can be attributed to two factors, quantum confinement and strain condition. First, quantum confinement in such narrow NWs definitely modifies the frequency of lattice vibrational modes as discovered by previous studies⁹⁻¹². However, since the whole diameter of our studied NWs is fixed, quantum confinement shall not be a major factor for the frequency shift observed in Fig. 1.

On the other hand, the internal strain of core-shell NWs induced by lattice mismatch can be an important reason for those frequency shifts. In our Si/Ge core-shell NWs, the Si part is stretched while the Ge part is compressed. As the core-shell size changes, the average lattice constant along the axial direction varies according to the Vegard's law ($a = a_A^0(1 - X) + a_B^0X$, where a is the lattice parameter of $A_{1-X}B_X$ crystal, X is the concentration of constituent element B, a_A^0 and a_B^0 are the lattice parameters of pure A and pure B crystals, respectively.), which can be seen from Table I. As a result, the intrinsic strain will gradually change, resulting in significant frequency shifts of Si and Ge modes.

To further confirm the above explanation, we focus on the frequency shifts of the particular optical modes picked from O_{Si} and O_{Ge} peaks, respectively. As shown in Fig. 3, for both Si-core/Ge-shell and Ge-core/Si-shell NWs, these frequency shifts are approximately linear to the square of the ratio of the core and NW radii, which is also proportional to the ratio of the number of atoms in the core and the whole NW. Since this linear relation is exactly the lattice constant variation according to the Vegard's Law, the change of the frequency shall be a result of the variation of the internal strain.

Meanwhile, we calculate homogenous Si NWs (SiNWs) and Ge NWs (GeNWs) with applied axial strain to check the strain effect as shown in Fig. 4. The size of homogenous NWs is chosen to be similar to the corresponding core size of Si/Ge core-shell NWs (SiGe-2 and GeSi-2 NWs in Table I) and we focus on the highest-frequency optical mode, which is the same mode plotted in Fig.

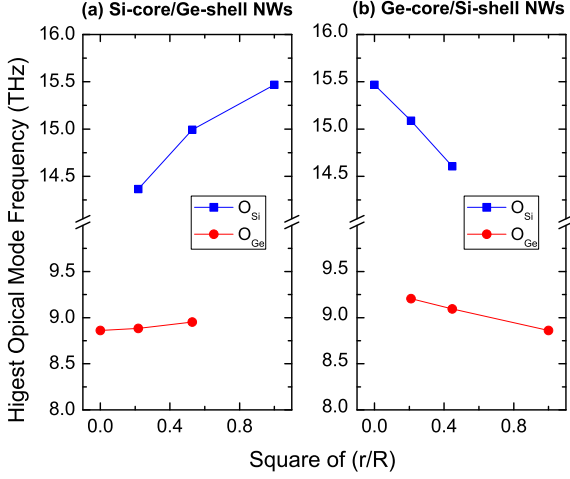


FIG. 3: The highest frequency of the optical mode picked from O_{Si} and O_{Ge} peaks. r is the core radius and R is the whole wire radius. (a) Si-core/Ge-shell NWs with a fixed wire diameter. (b) Ge-core/Si-shell NWs with a fixed wire diameter.

3. For both SiNW and GeNWs, these modes exhibit a monotonic change with the applied axial strain; their frequencies increase with the compressive strain and decrease with the tensile strain, which is consistent with the trend of the peak shifts in core-shell NWs. Moreover, we mark the highest-frequency optical mode of the corresponding core-shell NWs in Fig. 4. We find that their frequencies are close to those of the highest-frequency optical mode of homogenous NWs under the similar strain. Therefore, the variation of the strain condition is the main reason for the frequency shifts of high-frequency optical modes in core-shell NWs. This result builds a bridge to connect the frequency shift of characteristic optical modes with the structure of core-shell NWs.

B. Raman scattering spectrum

Raman scattering is a widely used approach to detect lattice vibrational modes of solids. Recently it is calculated in SiNWs as well^{12,13}. If the above frequency shifts of characteristic optical modes can be observed in their Raman scattering spectrum, it will be useful to understand the structures of core-shell NWs. Following the formulas in Eq. (2) and Eq. (3), we calculate the first-order Raman scattering spectra of our studied Si/Ge core-shell NWs and present them in Fig. 5.

In Fig. 5, we can see the following important features. First, those highest-frequency optical modes in the peaks O_{Si} and O_{Ge} are strongly active in the Raman scattering spectra. This is reasonable because they originate from bulk optical modes that are highly Raman active. Since we have shown that these shifts are caused by the strain and associated with structural variations,

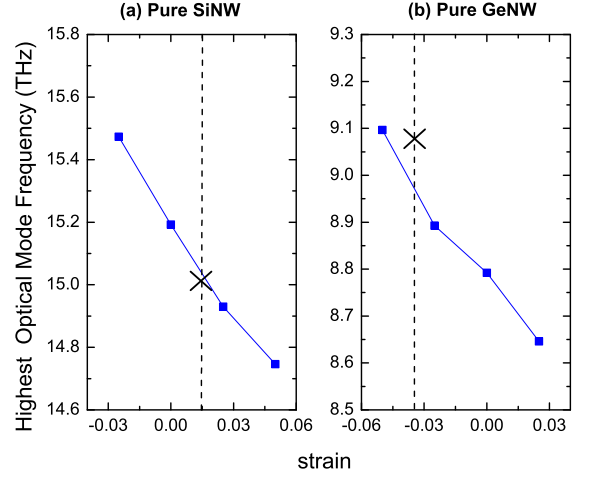


FIG. 4: Highest optical mode frequencies with external uniaxial strains applied to pure Si NW and pure Ge NW respectively. (a) Si-2 NW, the cross marks the frequency position of the highest Si optical mode in SiGe-2 NW. (b) Ge-2 NW, the cross marks the frequency position of the highest Ge optical mode in GeSi-2 NW.

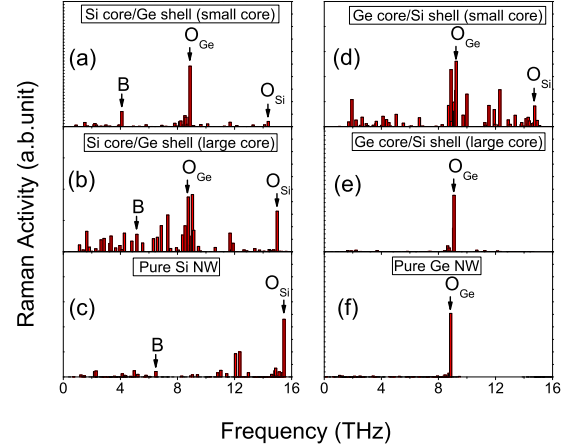


FIG. 5: Raman activity of Si/Ge core-shell NWs and homogeneous NWs. (a) SiGe-1 NW. (b) SiGe-2 NW. (c) Si-1 NW. (d) GeSi-1 NW. (e) GeSi-2 NW. (f) Ge-1 NW. O_{Si} marks the highest-frequency Si optical mode, O_{Ge} marks the highest-frequency Ge optical mode, and B marks the RBM.

the active Raman scattering peaks provide a convenient way to obtain structural information and corresponding strain condition inside Si/Ge core-shell NWs. As a result, they will be able to answer an fundamental question in nanoscience, which is if the huge strain can sustain in narrow core-shell NWs without introducing an significant amount of dislocations.

We also observe that the Raman scattering signal intensity strongly depends on the type of atoms involved in the vibrational modes. As shown in Fig. 5, those Ge

modes have much stronger Raman signals than those Si modes. This can be attributed to the larger size of Ge atoms, so that their motions can induce much stronger changes of polarizability, leading to enhanced Raman signals.

Meanwhile, the intensity of Raman scattering signals also depends on the spatial location of those atoms involved in the vibrational modes. The Raman scattering peak is usually enhanced if the corresponding mode is within the core region while it is depressed if the mode is within the shell region. For example, though SiGe-2 (Si core) NW has a lower proportion of Si atoms than GeSi-1 (Si shell) NW as listed in Table I, the relative Raman signal of the highest-frequency Si mode in SiGe-2 NW is stronger than that in GeSi-1 NW, as shown in Figs. 5 (b) and (d). The similar result can be observed in other NWs if we compare Figs. 5 (a) and (e).

Other than core-shell NWs, if comparing the Raman spectra of the homogenous SiNW and GeNW with a similar diameter as shown in Figs. 5 (c) and (f), we find that the SiNW, different from the GeNW which has only one dominant Raman peak at highest optical frequency, displays bright Raman activities for many phonon modes with lower frequencies. Since both bulk Si and Ge have only one dominant peak in the first-order Raman scatter spectrum, those newly active low-frequency modes in SiNWs imply that these vibrational modes are more affected by the quantum confinement and symmetry breaking in SiNWs. This has been observed by recent experiments^{9,10}. Such a different variation of vibrational modes may be helpful to explain why the thermal conductivity of SiNWs differs from their bulk crystals more than that of GeNWs²⁶.

C. RBM

After discussing the high-frequency optical vibrational modes in Si/Ge core-shell NWs, we turn to another type of collective modes: the RBM. Because of the unique geometry of quasi-one-dimensional nanostructures, their RBMs are of great interests and importance. For example, they are characteristic modes reflecting the geometry of carbon nanotubes^{27,28}. Recent research^{12,30} has also shown that the RBM are Raman active in narrow semiconducting NWs and they are tightly related to the diameter of NWs. Then an obvious question is whether we can observe the similar RBM in core-shell NWs.

Our first-principles result shows that the answer for core-shell NWs is more complicated than usual homogenous nanostructures case. For example, the RBM are identified in the Si-core/Ge-shell NWs studied in this work as shown in Fig. 6 (a). Moreover, we find that this RBM are Raman active and can be detected by the Raman scattering experiments, as marked in Fig. 5 (a), (b)

and (c). On the other hand, for the other type of NWs, Ge-core/Si-shell NWs, we cannot identify the RBM simply by sight. In fact, even for GeNWs with a similar

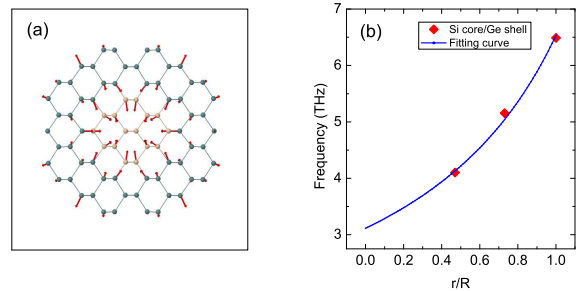


FIG. 6: (a) A typical RBM in Si/Ge core-shell NWs. (b) The frequency of RBM according to the core/wire size ratio. The fitting curve is based on Eq. (8).

diameter as the studied core-shell NWs, no RBM can be easily identified. The relative softer bonding between Ge atoms and the relatively larger mass of Ge atoms substantially reduce the frequency of the RBM. As a result, the RBM will mix with other modes because of the application of the sum rule in our simulations.

The most important motivation to study the RBM is to see if they have a strong relation with the structure of nanomaterials, such as the diameter of NWs. Previous studies¹² have successfully applied an elastic media model to study the RBM in SiNWs, encouraging us to apply a similar approach to study the RBM in Si-core/Ge-shell NWs. By using the classic wave equation with a cylindrical boundary condition and regarding core and shell regions as two different homogenous elastic medias with different sound velocities c_1 and c_2 respectively, the vibration of RBM can be described as $\vec{u}(x, y, z) = \vec{u}(x, y) = u(r)\hat{r}$ and satisfies the following equations:

$$\frac{\partial^2 u(r)}{\partial r^2} + \frac{1}{r} \frac{\partial u(r)}{\partial r} + \left(\frac{\omega^2}{c_1^2} - \frac{1}{r^2} \right) u(r) = 0 \text{ for } 0 \leq r \leq R_1, \quad (4a)$$

$$\frac{\partial^2 u(r)}{\partial r^2} + \frac{1}{r} \frac{\partial u(r)}{\partial r} + \left(\frac{\omega^2}{c_2^2} - \frac{1}{r^2} \right) u(r) = 0 \text{ for } R_1 \leq r \leq R_2, \quad (4b)$$

where ω is the frequency of RBM. R_1 is the core radius and R_2 is the shell radius, $u_1(r)$ and $u_2(r)$ are RBM wave function in the core and shell region, respectively. We solve Eqs. (4) using the free boundary condition at $r = R_2$ and continuous and differentiable continuous condition at $r = R_1$, we get the equation Eq. (5) which determine ω , the frequency of RBM:

$$c_1 J_1\left(\frac{\omega R_1}{c_1}\right) \left[Y_1'\left(\frac{\omega R_1}{c_2}\right) J_1'\left(\frac{\omega R_2}{c_2}\right) - Y_1'\left(\frac{\omega R_2}{c_2}\right) J_1'\left(\frac{\omega R_1}{c_2}\right) \right] + c_2 J_1'\left(\frac{\omega R_1}{c_1}\right) \left[Y_1'\left(\frac{\omega R_2}{c_2}\right) J_1\left(\frac{\omega R_1}{c_2}\right) - Y_1\left(\frac{\omega R_1}{c_2}\right) J_1'\left(\frac{\omega R_2}{c_2}\right) \right] = 0, \quad (5)$$

where J_1 and Y_1 are first-order Bessel functions of the first kind and second kind, respectively. By applying perturbation theory and the approximation of Bessel's functions in Eq. (6) when $x \gg \frac{3}{4}$ (it is satisfied in our simulations),

$$J_1(x) \approx \sqrt{\frac{2}{\pi x}} \cos\left(x - \frac{3}{4}\pi\right), \quad (6a)$$

$$Y_1(x) \approx \sqrt{\frac{2}{\pi x}} \sin\left(x - \frac{3}{4}\pi\right). \quad (6b)$$

Then a relation about the frequency of RBMs in core-shell NWs is obtained:

$$\omega\left(\frac{R_2}{c_2} + \frac{R_1}{c_1} - \frac{R_1}{c_2}\right) \approx \text{constant}. \quad (7)$$

Therefore, the frequency ω of the RBM is determined by the ratio of core/wire size and that of the sound velocities of core and shell. The constant in Eq. (7) are a series of values of x when $J_1'(x) = 0$, according to the free boundary condition. If we assume the sound velocity does not change too much, the above Eq. (7) can be approximated to

$$\omega \propto 1/\left[\frac{c_1}{c_2} + \frac{r}{R}\left(1 - \frac{c_1}{c_2}\right)\right]. \quad (8)$$

From the equation Eq. (7), we can easily reduce it to the known RBM frequency of homogenous NWs¹²:

$$\omega \frac{R}{c} \approx \text{constant}. \quad (9)$$

We have applied the equation Eq. (8) to fit the data of RBMs in the studied Si-core/Ge-shell NWs, as shown

in Fig. 6(b). From the fitting curve, the ratio of phonon group velocities in Si core and Ge shell is about 1.82, which is larger than the ratio in homogenous NWs or bulk materials (~ 1.56). This slight enlargement of the phonon group velocity ratio in core-shell NWs is a result of intrinsic strain effect and it may be of interest for thermoelectric applications of core-shell NWs.

IV. CONCLUSIONS

In summary, we have studied lattice vibrational modes of Si/Ge core-shell NWs by the first-principles approach. The frequency of high-energy Si-Si and Ge-Ge optical modes exhibits significant shifting when the core-shell size varies. Our analysis shows that these shifts are related to the variation of the strain conditions inside core-shell NWs. At the same time, the RBM are identified in the Si-core/Ge-shell NWs, whose frequency strongly depends on the geometry of NWs, and our elastic media model explains well the frequency of the RBM. Moreover, we have performed the calculation to obtain the first-order Raman scattering spectra of studied NWs, in which the shift of high-frequency optical modes and the RBM can be identified, providing a convenient way to detect the structural information of core-shell NWs. Our studied vibrational modes and their frequencies could be useful for thermoelectric applications as well.

Acknowledgments

Support from the International Center for Advanced Renewable Energy and Sustainability (I-CARES) is gratefully acknowledged. We acknowledge computational resource support by the Lonestar of Teragrid at the Texas Advanced Computing Center (TACC) and the National Energy Research Scientific Computing Center (NERSC) funded by the U.S. Department of Energy.

¹ L. J. Lauhon, M. S. Gudiksen, D. Wang and C. M. Lieber, Nature **420**, 57 (2002).
² J. Xiang, W. Lu, Y. Hu, Y. Wu, H. Yan and C. M. Lieber, Nature **441**, 489 (2006).
³ B. Tian, X. Zheng, T. J. Kempa, Y. Fang, N. Yu, G. Yu, J. Huang, C. M. Lieber, Nature **449**, 885 (2007).
⁴ G. Q. Zhang, W. Wang, and X. G. Li, Adv. Mater. **20**, 3654 (2008).
⁵ M. Hu, K. P. Giapis, J. V. Goicochea, X. Zhang, and D.

Poulikakos, Nano Lett. **11**(2), 618 (2011).

⁶ J. Chen, G. Zhang, B. Li, J. Chem. Phys. **135**, 104508 (2011).

⁷ M. Hu, X. Zhang, K. P. Giapis, D. Poulikakos, Phys. Rev. B **84**, 085442 (2011).

⁸ M. C. Wingert, Z. C. Y. Chen, E. Dechaumphai, J. Moon, J. Kim, J. Xiang, R. Chen, Nano Lett. **11**, 5507 (2011).

⁹ R. Wang, G. Zhou, Y. Liu, S. Pan, H. Zhang, D. Yu, Z. Zhang, Phys. Rev. B **61**, 16827 (2000).

- ¹⁰ K. W. Adu, H. R. Gutierrez, U. J. Kim, G. U. Sumanasekera, P. C. Eklund, *Nano Lett.* **5**(3), 409 (2005).
- ¹¹ H. Peelaers, B. Partoens and F.M. Peeters, *Appl. Phys. Lett.* **95**, 122110 (2009)
- ¹² L. Yang, M. Y. Chou, *Nano Lett.* **11**, 2618 (2011).
- ¹³ T. Thonhauser and G. D. Mahan, *Phys. Rev. B* **71**, 081301 (2005).
- ¹⁴ P. Hohenberg and W. Kohn, *Phys. Rev.* **136**, 864 (1964).
- ¹⁵ W. Kohn and L. J. Sham, *Phys. Rev.* **140**, 1133 (1965).
- ¹⁶ P. Giannozzi *et al.*, *J. Phys. Condens. Matter* **21**, 395502 (2009).
- ¹⁷ M. L. Cohen, M. Schluter, J. R. Chelikowsky, S. G. Louie, *Phys. Rev. B* **12**, 5575 (1975).
- ¹⁸ N. Troullier and J. L. Martins, *Phys. Rev. B* **43**, 1993 (1991).
- ¹⁹ Y. Wu, Y. Cui, L. Huynh, C. J. Barrelet, D. C. Bell and C. M. Lieber, *Nano Lett.* **4**, 433 (2004).
- ²⁰ S. Baroni, R. Resta, *Phys. Rev. B* **33**, 5969 (1986).
- ²¹ S. Baroni, P. Giannozzi, A. Testa, *Phys. Rev. Lett.* **58**, 1861 (1987).
- ²² P. Giannozzi, S. de Baroni, P. Ravone, S. Baroni, *Phys. Rev. B* **43**, 7231 (1991).
- ²³ X. Gonze, D. C. Allan, M. P. Teter, *Phys. Rev. Lett.* **68**, 3603 (1992).
- ²⁴ *Light Scattering in Solids II*, edited by M. Cardona and G. Guntherodt (springer-Verlag, Berlin, 1982).
- ²⁵ *Phonons: Theory and Experiments II*, edited by P. Bruesch (springer-Verlag, Berlin, 1986).
- ²⁶ M. Hu, X. Zhang, K. P. Giapis, D. Poulidakos, *Phys. Rev. B* **84**, 085442 (2011).
- ²⁷ C. Fantini, A. Jorio, M. Souza, M. S. Strano, M. S. Dresselhaus, M. A. Pimenta, *Phys. Rev. Lett.* **93**, 147406 (2004).
- ²⁸ A. G. Souza Filho *et al.*, *Phys. Rev. B* **69**, 115428 (2004).
- ²⁹ J. Zou and A. Balandin, *J. Appl. Phys.* **89**, 2932 (2001).
- ³⁰ E. Bourgeois, M.-V. Fernández-Serra, X. Blase, *Phys. Rev. B* **81**, 193410 (2010).